International Journal of Non-Linear Mechanics 102 (2018) 41–52

Contents lists available at ScienceDirect

International Journal of Non-Linear Mechanics

journal homepage: www.elsevier.com/locate/nlm

Analytical and numerical bifurcation analysis of dislocation pattern formation of the Walgraef–Aifantis model

Konstantinos G. Spiliotis [a], Lucia Russo [b,*], Constantinos Siettos [c,*], Elias C. Aifantis [a,d,e,f,g]

[a] Laboratory of Mechanics and Materials, Aristotle University of Thessaloniki, 54124 Thessaloniki, Greece
[b] Istituto di Ricerche sulla Combustione, Consiglio Nazionale delle Ricerche, Naples, Italy
[c] School of Applied Mathematics and Physical Sciences, National Technical University of Athens, 15780, Athens, Greece
[d] Michigan Technological University, Houghton, MI 49931, USA
[e] ITMO University, St. Petersburg 197101, Russia
[f] Togliatti State University, Togliatti 445020, Russia
[g] Beijing University of Civil Engineering and Architecture, Beijing 100044, China

ARTICLE INFO

Keywords:
Dislocations
Pattern formation
Turing instabilities
Numerical analysis

ABSTRACT

We analyze the pattern formation due to dislocations under cyclic loading resulting from the Walgraef–Aifantis model. The model consists of a set of partial differential equations of the reaction–diffusion type in the one dimensional finite space with two different diffusion-like coefficients, for the mobile (free to move when the applied resolved shear stress in the slip plane exceeds a certain threshold) and for the immobile (of slow movement or trapped) dislocations. We derive analytically the Turing spatial and Andronov–Hopf temporal instabilities emanating from the homogeneous solutions and construct the complete bifurcation diagram of the far-from-equilibrium spatio-temporal patterns, with respect to the applied stress and the size of the domain. Finally, we analyze the symmetric properties of all branches of both steady and oscillating far-from-equilibrium regimes.

1. Introduction

Dislocation patterning is a complex process governed by the multi-scale dynamic interactions ranging from the atomistic and microscopic to the meso and macroscopic scales. Different types of structures of cells, veins, deformation bands, persistent slip bands and cracks are among the characteristic patterns that have been observed [1–6]. From a dynamics point of view, the emergent behavior is highly nonlinear, including multiplicity of patterns, traveling waves, spatio-temporal oscillations and spatio-temporal chaos [3–8]. These far-from-equilibrium phenomena [2–5,9] emerge due to the complex interplay between inherent nonlinearities, diffusion-like transport and creation–annihilation feedback mechanisms. Some experimental evidence of such nonlinear behavior and pattern formation dislocation phenomena can be found for example in [10]. The analysis of such emergent behavior, dictates the use of modeling and analysis methodologies from the complex systems theory. Depending on the scale of the physical description, several approaches have been employed for modeling material behavior including dislocation phenomena: Density Functional Theory (DFT) [11–13] at the subatomic level, Molecular Dynamics (MD) [14,15] at the atomistic-nanoscale level, as well as Discrete Dislocation Dynamics (DDD) [16–20] at the microscopic/mesoscopic level. At the macroscopic/continuum level, the description comes most commonly in the form of Partial Differential Equations (PDEs) modeling the evolution of the system at hand. For crystalline materials with continuous distributed dislocations, such PDEs may be derived for densities of various families taking into account several microscopic properties such as creation, annihilation, diffusive-like transport and generalized reactions for dislocations and other structural defects [2–4,21]. On the level of analysis, the use of nonlinear dynamics techniques is necessary for identifying the mechanisms and establishing corresponding criteria that trigger phase transitions, which bring the system from equilibrium to far-from-equilibrium dislocations patterning and oscillations.

Over the last years, new theories and numerical schemes-codes have been developed for bridging the gap between detailed micro-mesoscopic (DDD) and macroscopic (at the level of continuum) descriptions. One of these approaches is based on statistics—statistical mechanics techniques [22–25] in 2 or 3 dimensions [26]. Starting with a simple description of the kinetic problem under the Peach and Koehler force, one can derive equations for the density of dislocations by averaging and using closures in the statistical evaluation of equations. Another important

* Corresponding authors.
E-mail addresses: l.russo@irc.cnr.it (L. Russo), ksiet@mail.ntua.gr (C. Siettos).

https://doi.org/10.1016/j.ijnonlinmec.2018.03.002
Received 8 November 2017; Received in revised form 27 February 2018; Accepted 7 March 2018
Available online 16 March 2018
0020-7462/© 2018 Published by Elsevier Ltd.

approach is the so call Continuous Dislocation Dynamics [27–30]. This approach takes into account geometrical properties of dislocations (dislocation curvatures) [27] and state equations for the evolutions of dislocations densities (total dislocation density, geometrically necessary density and the curvature density). Under this framework, the existence of dislocation patterning can be accomplished with respect to different parameters related to the external stress [28] and the type of loading [30].

In this paper, we analyze the pattern-formation dynamics of the initial Walgraef–Aifantis (WA) model [3,4,31,32] which has inspired many following works not only at the continuum but also at the meso and micro level of description [22–25,33]. In this connection it is noteworthy to mention that after 30 years of its appearance, it continues to drive developments in different disciplines [34,35]. The model consists of two reaction–diffusion-like type PDEs with a polynomial cubic nonlinearity in the one dimensional finite domain.

It is well known that reaction–diffusion PDEs can produce rich complex dynamic phenomena emerging from the interplay between the nonlinear reaction part and the diffusion process [36–52]. In his seminal work, Turing provided analytical results on the spatially periodic patterns (also known as Turing patterns) in reaction–diffusion PDEs arising from the homogeneous states [38]. More recently, it has been shown that Turing patterns oscillating in time can be generated through the interaction of Turing and Andronov–Hopf instabilities [39]. Alternatively, Turing patterns with periodicity in time may appear by coupling stationary Turing structures with oscillating layers [40], or in some bistable systems [41] in which neither Andronov–Hopf nor traveling-wave instabilities are required for their appearance. Moreover, diffusion-induced chaos has been also a subject of investigation for its importance to explain chemical chaos [42] and some complex biological phenomena [42,43].

For such systems, linear stability analysis has been widely applied to find critical conditions for the emergence of Turing patterns [44]. However, Turing patterns may experience secondary bifurcations leading to oscillating solutions far-from-equilibrium, as well as spatio-temporal chaos where nonlinearities have a dominant role not only on stabilizing a pattern, but also in producing unsuspected bifurcations. For these instabilities, the only way to detect the critical conditions for the appearance of such complex behavior is a systematic numerical bifurcation analysis [53–59].

Here, we construct the full bifurcation diagram of the WA model in the one dimensional finite domain with respect to the shear stress and the size of the domain. First, we conduct a linear stability analysis by considering spatial–temporal perturbations of the homogeneous equilibrium state. The conditions for complex spatial patterning, namely Turing instabilities and Andronov–Hopf bifurcations (as they have been also produced by Glazov [60]), which mark the onset of time-periodic formation are extracted analytically. Furthermore, we performed numerical bifurcation analysis with respect to the shear stress and the length of the domain to track branches of both stable and unstable far-from-equilibrium patterns. Finally, we study the symmetry and symmetry-breaking properties of the resulting solutions. This analysis is important as in far-from-equilibrium states, self-organized complex phenomena are often coupled with symmetry-breaking bifurcations.

2. Description of the WA model

Dislocations can be divided into two broad categories: (a) the mobile (free to move due to stress in the slip plane) and, (b) the immobile dislocations (of slow movement or trapped ones). Let $\rho_m(x,t)$ and $\rho_i(x,t)$ be the mobile and immobile, respectively, dislocation densities for the two types of dislocations in space x and time t. By applying a shear stress, the structure changes due to the dislocation movement and interactions.

For both types of dislocations, we impose balance equations according to the following rules:

1. Both mobile and immobile dislocation move, due to a fatigue cycle, in a diffusive-like way. Immobile or trapped dislocations due to limited movability have a lower diffusion-like coefficient with respect to the mobile ones. The diffusion-like term for both types of dislocations is addressed with the Laplace operator $D\nabla^2\rho_k$, $k = i,m$. It should be emphasized that generally, as also noted in [61], the D-coefficients in the model are not like the usual diffusivities. They depend on the local shear strain rate or dislocation velocity which in turn depends on the applied stress, thus the corresponding terms are stress driven and as such the dislocation motion is not diffusive (however in the initial WA model that we analyze here, these are constants). A more general discussion on this aspect can be found in [31,61].
2. Immobile dipoles capture the mobile dislocations, resulting to a sink and a source term of the form $\gamma\rho_i^2\rho_m$ in the mobile and immobile categories, respectively ($\gamma > 0$ is the rate of transformation from mobile to immobile and vice versa). The phenomenological nonlinear term $\gamma\rho_i^2\rho_m$ reflects the microscopic rule according to which two immobile dislocations (in the form of immobile dipoles) represented by ρ_i^2 can trap another mobile ρ_m dislocation. Higher nonlinearities of the form $\rho_m\rho_i^n$ (representing a wall of dipoles) can be also considered without qualitatively changes [31].
3. During the Persistent Slip Bands (PSB) formation, a large number of dipoles (already existing in the veins) are pinned up almost immediately after the produced dislocation. This phenomenon is addressed by adding a source term of the form$g\left(\rho_i\right) = C - a\rho_i = a\rho_{0i} - a\rho_i$ where a represents the annihilation rate of slow (immobile) dislocations and ρ_{0i} is the initial density of immobile dislocations [3,4,32].
4. Immobile dislocations are freed from the forest of dislocations by the applied stress. This process introduces a linear source term $\beta\rho_i$ in the mobile balance equation. The β parameter expresses the rate of dislocation freeing from the forest. This parameter is related to the applied external stress, mimicking the destabilization of dislocations dipoles under stress. Various experiments [62] and numerical simulations of DDD models for example in BCC [62,63] have shown a critical value of the stress where the dislocation dipoles become unstable. According to the results presented in [63] the regions of stabilization–destabilization depend on the positions of dislocations, their mobility velocity but mainly on the external forces. In our analysis, β is considered to be space independent.

The previous rules may be described mathematically at the continuum level under certain assumptions [3,4] with the following system of non-linear partial differential equations:

$$\begin{cases} \dfrac{\partial\rho_i}{\partial t} = D_i\dfrac{\partial^2\rho_i}{\partial x^2} + a\rho_{0i} - a\rho_i - \beta\rho_i + \gamma\rho_m\rho_i^2 \\ \dfrac{\partial\rho_m}{\partial t} = D_m\dfrac{\partial^2\rho_m}{\partial x^2} + \beta\rho_i - \gamma\rho_m\rho_i^2 \end{cases} \tag{1a}$$

where D_i, D_m are the immobile and mobile diffusion-like constants, respectively. For a finite domain of size L, no flux boundary conditions are assumed i.e.

$$\frac{\partial\rho_k}{\partial x}(0,t) = \frac{\partial\rho_k}{\partial x}(L,t) = 0, \quad k = i,m. \tag{1b}$$

3. Stability analysis of the homogeneous solutions: analytical results

Homogeneous equilibrium solutions, resulting from Eq. (1a) are obtained by setting the densities equal to constants, i.e. $\rho_i = c_i$ and $\rho_m = c_m$. Then Eq. (1) reads

$$\begin{cases} 0 = 0 + a\rho_{0i} - ac_i - \beta c_i + \gamma c_i^2 c_m \\ 0 = 0 + \beta c_i - \gamma c_i^2 c_m \end{cases} \Rightarrow \begin{cases} 0 = a\rho_{0i} - (a+\beta)c_i + \gamma c_i\dfrac{\beta}{\gamma} \\ \dfrac{\beta}{\gamma c_i} = c_m \end{cases}$$

$$\Rightarrow \begin{cases} c_i = \rho_{0i} \\ c_m = \dfrac{\beta}{\gamma c_i} = \dfrac{\beta}{\gamma\rho_{0i}}. \end{cases} \tag{2}$$

We perturb the homogeneous solutions as

$$\begin{cases} \rho_i = c_i + \xi(x,t) \\ \rho_m = c_m + \eta(x,t). \end{cases} \tag{3}$$

Substituting Eq. (3) into Eq. (1a), we obtain the following linearized system for the perturbation vector $\boldsymbol{U} = (\xi, \eta)^T$

$$\begin{pmatrix} \frac{\partial \xi}{\partial t} \\ \frac{\partial \eta}{\partial t} \end{pmatrix} = \boldsymbol{J} \begin{pmatrix} \xi \\ \eta \end{pmatrix} + \boldsymbol{D} \begin{pmatrix} \nabla^2 \xi \\ \nabla^2 \eta \end{pmatrix} \tag{4a}$$

where $\boldsymbol{J} = \begin{pmatrix} -(\beta + a) + 2\gamma c_i c_m & \gamma c_i^2 \\ \beta - 2\gamma c_i c_m & -\gamma c_i^2 \end{pmatrix} = \begin{pmatrix} \beta - a & \gamma \rho_{0i}^2 \\ -\beta & -\gamma \rho_{0i}^2 \end{pmatrix}$ is the Jacobian matrix and $\boldsymbol{D} = \begin{pmatrix} D_i & 0 \\ 0 & D_m \end{pmatrix}$ is the matrix of the diffusion-like coefficients. The boundary conditions read:

$$\boldsymbol{U}_x(0,t) = \boldsymbol{U}_x(L,t) = 0. \tag{4b}$$

By separation of variables in time and space, we seek solutions of the form $\boldsymbol{U} = T(t)\boldsymbol{X}(x)$ which result to the following expressions for the spatial component $\boldsymbol{X}$ and the temporal component T:

$$\begin{cases} T = e^{\lambda t} \\ \boldsymbol{X} = \begin{pmatrix} c_1 \cos \frac{n\pi x}{L} \\ c_2 \cos \frac{n\pi x}{L} \end{pmatrix} \end{cases} \Leftrightarrow \begin{cases} T = e^{\lambda t} \\ \boldsymbol{X} = \cos \frac{n\pi x}{L} \begin{pmatrix} c_1 \\ c_2 \end{pmatrix} \equiv \boldsymbol{C} \cos \frac{n\pi x}{L}, \\ n = 0, 1, 2, 3, \ldots. \end{cases} \tag{5}$$

For a nontrivial solution, the following condition must be satisfied:

$$\begin{aligned} \det(\boldsymbol{A}) = \det\left[\boldsymbol{D}\left(\frac{n\pi}{L}\right)^2 - (\boldsymbol{J} - \lambda \boldsymbol{I})\right] = 0 \Leftrightarrow \\ \lambda^2 + \lambda\left(\gamma\rho_{0i}^2 - \beta + a + (D_i + D_m)\left(\frac{n\pi}{L}\right)^2\right) + \gamma\rho_{0i}^2 a \\ + \gamma\rho_{0i}^2 D_i\left(\frac{n\pi}{L}\right)^2 - (\beta - a) D_m\left(\frac{n\pi}{L}\right)^2 + D_i D_m\left(\frac{n\pi}{L}\right)^4 = 0. \end{aligned} \tag{6}$$

The steady state is stable if for each $n = 0, 1, 2, \ldots$ the following conditions hold

$$\begin{cases} -\left(\gamma\rho_{0i}^2 - \beta + a + (D_i + D_m)\left(\frac{n\pi}{L}\right)^2\right) < 0 \\ and \qquad n = 0, 1, 2, \ldots \\ \gamma\rho_{0i}^2 a + \gamma\rho_{0i}^2 D_i\left(\frac{n\pi}{L}\right)^2 - (\beta - a) D_m\left(\frac{n\pi}{L}\right)^2 \\ \quad + D_i D_m\left(\frac{n\pi}{L}\right)^4 > 0. \end{cases} \tag{7}$$

Hence, the steady state is stable if $\mathrm{Re}(\lambda_1), \mathrm{Re}(\lambda_2) < 0$.

4. Turing and Andronov–Hopf instabilities: analytical results

The spatial component $\boldsymbol{X}$ is bounded and the temporal component T has an exponential dependence on λ. If $\mathrm{Re}(\lambda_1), \mathrm{Re}(\lambda_2) < 0$ the perturbation decays, thus implying stable solutions. Otherwise if for one exponent $\mathrm{Re}(\lambda) > 0$ the homogeneous solution is unstable.

Since Eq. (6) is a second order polynomial, the stability of the homogeneous solution can be lost in favor of more complex spatial–temporal structures in two ways induced by diffusive-like transport: (a) through Turing, or, (b) Andronov–Hopf bifurcations, which we examine below.

4.1. Turing bifurcations

Turing instabilities arise when one leading real eigenvalue crosses zero [44]. Hence, the constant part of Eq. (6) is zero i.e. there is at least one $n \in N$ such that

$$\gamma\rho_{0i}^2 a + \gamma\rho_{0i}^2 D_i\left(\frac{n\pi}{L}\right)^2 - (\beta - a) D_m\left(\frac{n\pi}{L}\right)^2 + D_i D_m\left(\frac{n\pi}{L}\right)^4 = 0. \tag{8}$$

The above equation can be solved with respect to β (the stress parameter) or L (the size of the domain). Considering β as the bifurcation parameter one obtains from Eq. (8) that the critical value for the appearance of Turing instability is

$$\beta_T = a + \frac{a\gamma\rho_{0i}^2 L^2}{D_m (n\pi)^2} + D_i\left(\frac{n\pi}{L}\right)^2 + \frac{D_i}{D_m}\gamma\rho_{0i}^2, \; n = 1, 2, 3 \ldots. \tag{9}$$

Since, Eq. (9) is not valid for the mode resulting for $n = 0$, we examine separately the $n = 0$ case with the aid of Eq. (8). When $n = 0$, we have from Eq. (8) that $\gamma\rho_{0i}^2 a = 0$ which is a contradiction as it is assumed that $\gamma, \rho_{0i}, a > 0$; hence the mode corresponding to $n = 0$ cannot induce Turing instabilities.

Of particular interest is the minimum value of β, say β_T, with respect to the natural number n, which indicates the first time of stability loss (see Fig. 1). Following [36,60] we regard the critical β_T as a function of n i.e. $\beta_T = \beta_T(n)$ and setting $\frac{d\beta_T}{dn} = 0$ we obtain the characteristic wavelength

$$n_0 = \left(\frac{a\gamma}{D_m D_i}\right)^{1/4} \frac{\sqrt{\rho_{0i}} L}{\pi} \tag{10}$$

and the corresponding minimum:

$$\beta_T(n_0) = \left(\sqrt{a} + \sqrt{\frac{D_i}{D_m}}\gamma\rho_{0i}\right)^2. \tag{11}$$

The pair $(n_0, \beta_T(n_0))$ corresponds to the minimum point shown in Fig. 1.

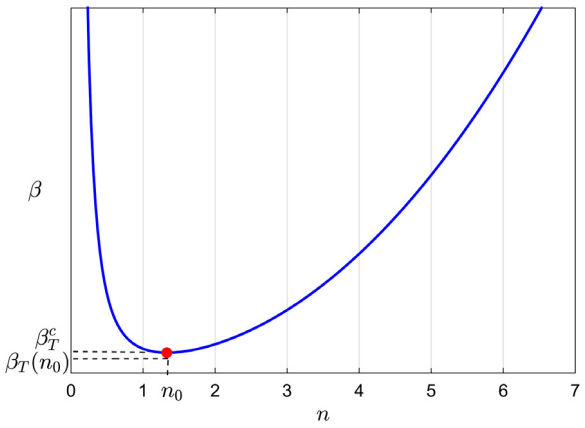

Fig. 1. The β_T as a function of n. The red filled circle marks the minimum $\beta_T(n_0)$ resulting from the characteristic wave length n_0. The critical value β_T^C indicates dynamic transitions via Turing points and it is defined as the nearest to $\beta_T(n_0)$.

Since $n \in N$, we set as n^*, the natural number which gives the value of parameter $\beta_T^C = \beta_T(n^*)$ closest to the minimum $\beta_T(n_0)$ (see Fig. 1 and the analysis presented in [36]). The critical value $\beta_T^C = \beta_T(n^*)$ indicates the onset of a Turing instability and n^* is the first mode, which this instability occurs (see Fig. 1). The characteristic wavelength depends on L and reflects the size effect in contrast with the infinite domain where the characteristic wavelength is independent from L [3].

Hence, setting $n_0 = 1$ in Eq. (10) we conclude that the size of the domain L that corresponds to the minimum value β_T is

$$L^* = \frac{\pi}{\sqrt{\rho_{0i}}}\left(\frac{D_i * D_m}{a\gamma}\right)^{1/4}. \tag{12}$$

We remark here, that the above analysis predicts that the minimum β_T (Eq. (11)) is independent on the size L of the domain. As discussed in Section 5, this is actually an artifact as the above analysis treats n as a real number.

4.2. Andronov–Hopf bifurcations

Similar to the previous analysis, the homogeneous steady state solution may lose its stability by giving rise to periodic solutions through

an Andronov–Hopf bifurcation. This occurs when two eigenvalues computed from Eq. (6) pass the imaginary axis, i.e. there is at least one natural $n \in N$ such that

$$\gamma\rho_{0i}^2 - \beta + a + \left(D_i + D_m\right)\left(\frac{n\pi}{L}\right)^2 = 0. \tag{13}$$

Again, Eq. (13) can be solved with respect to β or the size of the domain L. Choosing β as the bifurcation parameter, the critical value resulting from Eq. (13) is:

$$\beta_H = \gamma\rho_{0i}^2 + a + \left(D_i + D_m\right)\left(\frac{n\pi}{L}\right)^2. \tag{14}$$

The value of β_H depends on the natural number n monotonically, therefore this kind of instability takes place for the first time when $n = 0$ at:

$$\beta_H^C = \gamma\rho_{0i}^2 + a. \tag{15}$$

We mention here that the critical β_H^C given by Eq. (15) is the same as the one found in [3,60] for the case of the infinite domain. Thus, the size effect enters only in the occurrence of Turing instabilities and not in the Andronov–Hopf bifurcations on the homogeneous solutions as may be expected.

5. Size effect analysis

As discussed in Section 4.1 the minimum value of n to get Turing instabilities (in the small size case) around (and for smaller values of) the critical value L^* (see Eq. (12)) is $n = n^* = 1$. Thus, if we substitute $n = 1$ to Eq. (9) we get

$$\beta_T^C = \beta_T(1) = a + \frac{a\gamma\rho_{0i}^2 L^2}{D_m\pi^2} + D_i\left(\frac{\pi}{L}\right)^2 + \frac{D_i}{D_m}\gamma\rho_{0i}^2. \tag{16}$$

Comparing Eq. (16) with Eq. (11), we note that the minimum value of the stress-like parameter for which one takes a Turing instability, clearly depends on L. As L gets smaller, the linear analysis of the model predicts that β_T^C grows inversely with L^2, meaning that for small sizes of the domain the stress dependent parameter β should be very large for the appearance of Turing instabilities. This is also confirmed experimentally in the work of [64–68] (see also the discussion in the Section of Conclusions).

Note that, as shown in Section 4.2, the minimum value of β_H^C (Eq. (15)) which gives rise to periodic instabilities is independent of L as this happens for $n = 0$. Consequently, the following two cases of dynamics come into play when we treat L as our bifurcation parameter for small sizes of the domain L (i.e. around the critical value L^*):
(A) Suppose that we set a value for the stress parameter β in the simulations such that $\beta_T^C(L) < \beta < \beta_H^C$ (Fig. 2(a)) meaning that a Turing instability has preceded and the homogeneous solution is unstable.

Now, as L decreases, the critical value β_T^C increases (but the homogeneous solution remains unstable). As β_T^C increases inversely with L^2 at some critical size we have that

$$\beta_T^C(L) = \beta \Leftrightarrow L \equiv L^C \tag{17}$$

(in Fig. 2(a) this is the intersection point of the lower black line with the red line at $n = 1$). Consequently, for $0 < L < L^C < L^* \Rightarrow \beta < \beta_T^C < \beta_H^C$, the homogeneous solution (through the Turing bifurcation) becomes stable. Eq. (17) is written as:

$$a + \frac{a\gamma\rho_{0i}^2 L^2}{D_m\pi^2} + D_i\left(\frac{\pi}{L}\right)^2 + \frac{D_i}{D_m}\gamma\rho_{0i}^2 = \beta, \tag{18}$$

which can be solved with respect to the size L to find L^C.
(B) Let us set a β such that $\beta_T^C(L) < \beta_H^C < \beta$ (Fig. 2(b)). Since β_T^C increases inversely with L^2, again at some critical value of L_1: $\beta_H^C = \beta_T^C(L_1)$ (in Fig. 2(b) this is the intersection point of the lower black line with the red line at $n = 1$). Continuing with lower values of L_1 we get a second critical L_2 where $\beta_H^C < \beta_T^C(L_2) = \beta$ (see in Fig. 2(b) the first red line up to the second black line). Then, for $L : 0 < L < L_2$ the system exhibits time periodic homogeneous solutions.

6. A proof of uniqueness of the constant solution in small specimens

We give a simple proof in one dimension that for a critical value L_0 and for all $L : L < L_0$ the only steady state is the thermodynamic homogeneous solution $\left(\rho_{0i}, \frac{\beta}{\gamma\rho_{0i}}\right)$.

We seek for steady states solutions of Eq. (1a), i.e. solutions of the system:

$$\begin{cases} 0 = D_i\dfrac{\partial^2\rho_i}{\partial x^2} + a\rho_{0i} - a\rho_i - \beta\rho_i + \gamma\rho_m\rho_i^2 \\ 0 = D_m\dfrac{\partial^2\rho_m}{\partial x^2} + \beta\rho_i - \gamma\rho_m\rho_i^2. \end{cases} \tag{19}$$

We set $y = \frac{x}{L}$ and $0 \le y \le 1$. Then $\frac{\partial^2\rho_i}{\partial x^2} = \frac{1}{L^2}\frac{\partial^2\rho_i}{\partial y^2}$ and $\frac{\partial^2\rho_m}{\partial x^2} = \frac{1}{L^2}\frac{\partial^2\rho_m}{\partial y^2}$ where the boundary conditions are $\frac{\partial\rho_k}{\partial y}(0,t) = \frac{\partial\rho_k}{\partial y}(1,t) = 0$, $k = i, m$. Hence, Eq. (19) takes the form:

$$\begin{cases} 0 = \dfrac{D_i}{L^2}\dfrac{\partial^2\rho_i}{\partial y^2} + a\rho_{0i} - a\rho_i - \beta\rho_i + \gamma\rho_m\rho_i^2 \\ 0 = \dfrac{D_m}{L^2}\dfrac{\partial^2\rho_m}{\partial y^2} + \beta\rho_i - \gamma\rho_m\rho_i^2. \end{cases} \tag{20}$$

By adding the above equations we get:

$$0 = \frac{D_i}{L^2}\frac{\partial^2\rho_i}{\partial y^2} + \frac{D_m}{L^2}\frac{\partial^2\rho_m}{\partial y^2} + a\rho_{0i} - a\rho_i. \tag{21}$$

Integrating Eq. (21) we get:

$$\int_0^1 \left(D_i\frac{\partial^2\rho_i}{\partial y^2} + D_m\frac{\partial^2\rho_m}{\partial y^2}\right) + L^2\left(\int_0^1 a\rho_{0i} - a\rho_i\right) = 0$$

and taking into account the boundary conditions of y we get

$$0 = \left[D_i\frac{\partial\rho_i}{\partial y} + D_m\frac{\partial\rho_m}{\partial y}\right]_0^1 = -\int_0^1 \left(a\rho_{0i} - a\rho_i\right). \tag{22}$$

Since ρ_{0i} is constant, Eq. (22) results to

$$\int_0^1 \rho_i = \int_0^1 \rho_{0i} = \rho_{0i}. \tag{23}$$

Following [69], we multiply by $\rho_i - \rho_{0i}$ the first of the two equations in Eq. (20) and integrate to receive

$$\begin{aligned} 0 = &\int_0^1 \left(\frac{D_i}{L^2}\frac{\partial^2\rho_i}{\partial y^2}\left(\rho_i - \rho_{0i}\right) + \left(a\rho_{0i} - a\rho_i\right)\left(\rho_i - \rho_{0i}\right)\right. \\ &\left. - \beta\rho_i\left(\rho_i - \rho_{0i}\right) + \gamma\rho_m\rho_i^2\left(\rho_i - \rho_{0i}\right)\right) \Rightarrow \\ &- \int_0^1 D_i\frac{\partial^2\left(\rho_i - \rho_{0i}\right)}{\partial y^2}\left(\rho_i - \rho_{0i}\right) \\ = L^2&\int_0^1 \left(\left(a\rho_{0i} - a\rho_i\right)\left(\rho_i - \rho_{0i}\right) - \beta\rho_i\left(\rho_i - \rho_{0i}\right) + \gamma\rho_m\rho_i^2\left(\rho_i - \rho_{0i}\right)\right) \Rightarrow \\ &- \left[D_i\frac{\partial\left(\rho_i - \rho_{0i}\right)}{\partial y}\left(\rho_i - \rho_{0i}\right)\right]_0^1 + \int_0^1 D_i\left(\frac{\partial\left(\rho_i - \rho_{0i}\right)}{\partial y}\right)^2 = \\ &L^2\int_0^1 \left(\left(a\rho_{0i} - a\rho_i\right)\left(\rho_i - \rho_{0i}\right) - \beta\rho_i\left(\rho_i - \rho_{0i}\right) + \gamma\rho_m\rho_i^2\left(\rho_i - \rho_{0i}\right)\right). \end{aligned}$$

Using the no flux boundaries conditions and Eq. (22) we have:

$$\begin{aligned} \int_0^L D_i\left(\frac{\partial\left(\rho_i - \rho_{0i}\right)}{\partial y}\right)^2 &= -L^2(\beta + a)\int_0^1 \left(\rho_i - \rho_{0i}\right)^2 \\ &+ L^2\int_0^1 \left(\gamma\rho_m\rho_i^2\left(\rho_i - \rho_{0i}\right)\right) \\ &\le L^2\int_0^1 \left(\gamma\rho_m\rho_i^2\left(\rho_i - \rho_{0i}\right)\right). \end{aligned}$$

The term inside the last integral, $\left(\gamma\rho_m\rho_i^2\left(\rho_i - \rho_{0i}\right)\right)$ is continuous in the closed interval $[0,1]$ implying that it takes maximum and minimum

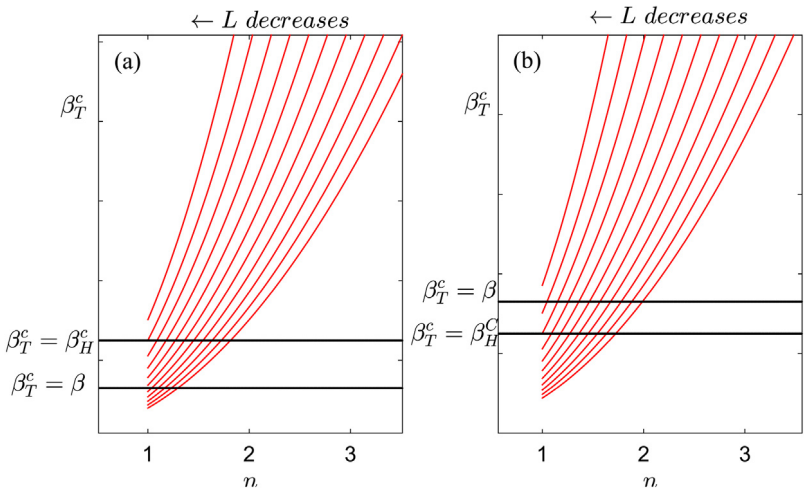

Fig. 2. Size effect in the (WA) dynamics. Red line is the β_T (Eq. (9)) as a function of n. The minimum value of β_T is denoted by β_T^C (in the small sizes L) resulting from $n = 1$. As the size L decreases the β_T^C ($n = 1$) value increases. (a) There is a critical value L^C where Eq. (17) holds, leading the dynamics to homogeneous solutions. (b) For $\beta_T^C > \beta > \beta_H^C$, the system displays homogeneous periodic solutions. (For interpretation of the references to color in this figure legend, the reader is referred to the web version of this article.)

values i.e. it is a bounded function. The last part of inequality converges to zero as L tends to zero:

$$\left| L^2 \int_0^1 \left(\gamma \rho_m \rho_i^2 \left(\rho_i - \rho_{0i} \right) \right) \right| \leq L^2 \int_0^1 \left| \gamma \rho_m \rho_i^2 \left(\rho_i - \rho_{0i} \right) \right| \leq L^2 \int_0^1 M = ML^2 \to 0.$$

Then:

$$0 \leq \int_0^1 D_i \left(\frac{\partial \left(\rho_i - \rho_{0i} \right)}{\partial y} \right)^2 \leq L^2 \int_0^1 M = ML^2 \to 0.$$

Hence, similar to [69] there is a $L_0 > 0$ such that for $0 < L < L_0$ we have $\frac{\partial(\rho_i - \rho_{0i})}{\partial y} = 0, \forall y \in [0, L]$. Immediately, we obtain $\rho_i = \rho_{0i}$. Finally, from Eq. (20) we take

$$-\beta \rho_i + \gamma \rho_m \rho_i^2 = 0 \Rightarrow \rho_m = \frac{\beta}{\gamma \rho_{0i}}.$$

7. Numerical bifurcation analysis

The nonlinear form of the WA model is prohibitive for the derivation of analytical closed form solutions. This dictates the use of numerical analysis for the systematic study of far-from-equilibrium branches of solutions in the parameter space. Thus, we performed numerical bifurcation analysis, in order to trace stable and unstable branches of steady state and periodic solutions and identify critical points which mark the onset of phase transitions far-from-equilibrium. For our computations, we used central finite differences for discretizing space and an explicit Runge–Kutta of 4th order as implemented by the ODE suite of Matlab with an adaptive step for the time integration. The one dimensional domain is discretized with $N = 100$ equidistant nodes. Denser discretization resulted to quantitatively equivalent outcomes.

Tracing of branches of fixed points through turning points in one parameter space, is achieved by augmenting the right-hand-side of the discretized PDE with the linearized pseudo arc-length continuation condition [53,54]:

$$N(\boldsymbol{u}, s) = \boldsymbol{a} \left(\boldsymbol{\rho} - \boldsymbol{\rho_0} \right) + b \left(\varepsilon - \varepsilon_0 \right) - \Delta s = 0. \tag{24}$$

$\Delta s = s - s_0$ is the pseudo arc-length continuation step and

$$\boldsymbol{a} = \frac{\boldsymbol{\rho}_1 - \boldsymbol{\rho}_0}{\Delta s} \quad \text{and} \quad b = \frac{\varepsilon_1 - \varepsilon_0}{\Delta s}. \tag{25}$$

$(\boldsymbol{\rho}_0, \varepsilon_0)$ and $(\boldsymbol{\rho}_1, \varepsilon_1)$ are two already computed solutions, which can be found for example at the start of the tracing procedure by temporal simulations. The stability of fixed points is determined by the eigenvalues λ_i of the Jacobian of the right-hand-side of the discretized PDE upon convergence of the Newton–Raphson iteration.

Periodical solutions are computed by augmenting the discretized system with a phase condition of the form

$$\left(\frac{d\boldsymbol{\rho}}{dt}, \frac{dT}{dt}, p(\boldsymbol{\rho}, \varepsilon) \right)^T = \left(f(\boldsymbol{\rho}, \varepsilon), 0, 0 \right)^T \tag{26}$$

where $p(\boldsymbol{\rho}, \varepsilon) = \int_0^T \boldsymbol{\rho}(t) \dot{\boldsymbol{\rho}}(t) dt = 0$, demanding that $\boldsymbol{\rho}(0) = \boldsymbol{\rho}(T)$ [53,55–57]. The stability of periodic solutions is determined by the eigenvalues of the corresponding monodromy matrix [53,55–57].

Following [3,4,70] the dislocation densities range in our simulations from $10^{12} - 10^{14}$ m^{-2} for both the immobile and mobiles dislocations. The ratio of diffusion-like coefficients should be at most 10^{-2} i.e. $\frac{D_i}{D_m} \leq 10^{-2}$ [3,4,70]. For our simulations, we have set $D_i = 0.01$ and $D_m = 1$ (μm^2/s). The mean velocity of mobile dislocation is related with the corresponding diffusivity as $D_m \approx \frac{v_m^2}{2\gamma\rho_{0i}^2}$ [70], and it ranges from $10^{-8} - 10^{-3}$ m/s. The parameter a representing the annihilation rate of the source function g was set $a = 1$, and $\gamma = 1$.

7.1. The effect of the shear stress

We performed several simulations with different initial conditions as the (shear stress dependent) parameter β varies and we observed a rich nonlinear dynamical behavior. Fig. 3 shows the temporal evolution of the immobile dislocation density for various values of the shear stress. For $\beta = 0.1$ the system goes to a steady state (see Fig. 3a). As the value of β increases to 1.21 a new time-invariant inhomogeneous solution appears (Fig. 3b), while the homogeneous solution loses its stability. For higher values of the shear stress, a new inhomogeneous steady state solution appears (Fig. 3c), while for even higher values of β periodic solutions emerge (Fig. 3d). The above observations indicate the presence of criticalities marking the onset of far-from-equilibrium phase-transitions.

The bifurcation diagram with respect to the shear stress that explains the above mentioned dynamics is shown in Fig. 4. Here, the y-axis corresponds to maximum and minimum values of the density of immobile dislocations ρ_i.

In the interval $0.1 \leq \beta \leq 1.21$, the homogeneous equilibrium is stable (e.g. for $\beta = 1.14$ such a profile is shown in Fig. 5a). As the value of

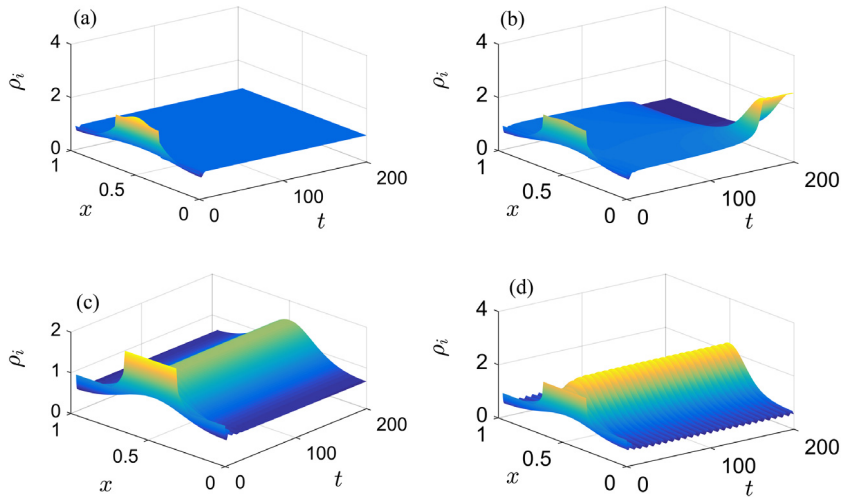

Fig. 3. Profiles of the immobile density resulting from time integration and for different values of the parameter β. (a) For $\beta = 0.1$ the immobile density returns fast to the homogeneous solution. (b) For $\beta = 1.2$ an inhomogeneous solution coexists with the homogeneous solution. (c) For $\beta = 1.43$ a new stable inhomogeneous solution appears. (d) For $\beta = 1.8$ a periodic solution exists.

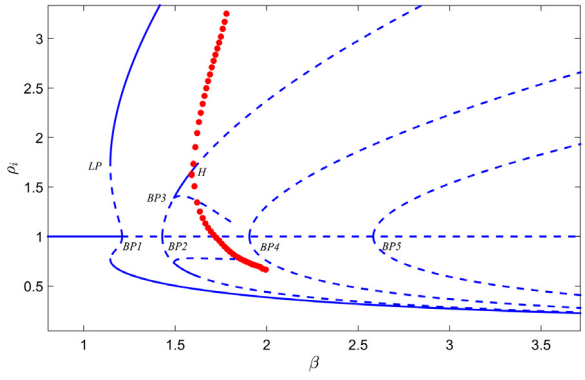

Fig. 4. Bifurcation diagram with respect to the parameter β (shear stress) of the WA model. Solid (dashed) lines correspond to stable (unstable) solutions. Periodic inhomogeneous solutions emerge via an Andronov–Hopf bifurcation (red circles depict the maxima and minima of the corresponding limit cycles).

β increases beyond a critical value around $\beta = 1.21$, the homogeneous-flat solution loses its stability through a subcritical pitchfork bifurcation (marked as ($BP1$) in Fig. 4) giving birth to two new unstable branches of solutions. There, one eigenvalue becomes positive, thus marking the onset of a Turing instability. The solutions of the new born branches bifurcate again via a turning point at $\beta = 1.146$ (marked as (LP) in Fig. 4), where they become stable. It should be noted that between $\beta = 1.146$ and $\beta = 1.121$, there is a multiplicity of three stable regime solutions: the two inhomogeneous solutions (which are asymmetric and conjugate as it will be discussed in the section of symmetry analysis) and the homogeneous solution. A representative profile related to the one of the two inhomogeneous branches for $\beta = 1.4$ is shown in Fig. 5b. For higher values of β and at the critical value $\beta = 1.42$ (marked as ($BP2$) in Fig. 4), a new branch of unstable inhomogeneous steady state solutions arise from the homogeneous steady state regime. A representative profile for $\beta = 1.45$ is shown in Fig. 5c. On this new branch, the inhomogeneous regime regains stability at $\beta = 1.492$ ($BP3$) and a pair of two asymmetric solutions appear. Furthermore, on this branch, at $\beta = 1.601$, a stable branch of limit cycles (periodic inhomogeneous solutions) arises via an Andronov–Hopf bifurcation. Oscillating profiles within the oscillating regime for $\beta = 1.8$ are depicted in Fig. 5d.

Increasing the value of the shear stress, another pitchfork bifurcation (marked as ($BP4$) in Fig. 4), occurs on the homogeneous branch at $\beta = 1.9055$ giving birth to two new unstable branches of inhomogeneous solutions. A representative profile for $\beta = 3.5$ is shown in Fig. 5e. A further increase of the shear stress brings to a similar transition at another pitchfork bifurcation point (marked as ($BP5$) in Fig. 4), where two new branches of unstable inhomogeneous solutions arise. A representative profile on this branch for $\beta = 3.88$ is shown in Fig. 5f.

Linear stability analysis predicts (see Section 4) the first critical point which marks the loss of stability of the homogeneous solutions. For the specific values of the parameters, Eq. (12) gives $L^* = \frac{\pi}{\sqrt{\rho_{10}}}\left(\frac{D_i * D_m}{a\gamma}\right)^{1/4} = 0.9935$, meaning that Eq. (11) is valid for $L = 1$ and thus the critical value for the first loss of stability is given by $\beta_T\left(n_0\right) = \left(\sqrt{a} + \sqrt{\frac{D_i}{D_m}\gamma\rho_{0i}}\right)^2 = \left(1 + \sqrt{0.01}\right)^2 = 1.21$ i.e. $\beta_T^C = 1.21$, which is in excellent agreement with the numerical bifurcation results.

7.2. The size effect

The resulting bifurcation diagram with respect to the size L of the domain is depicted in Figs. 6 and 7. As discussed in Section 5, the decrement of size L leads the system to a unique equilibrium, i.e. the homogeneous steady states regime. Fig. 8 depicts representative profiles of solutions along the branches of the bifurcation diagram. The shear stress was set equal to $\beta = 1.8$. In the range $0.1 \leq L \leq 0.3564$ only the homogeneous solution exists (a representative profile at $L = 0.248$ is shown in Fig. 8a).

As L increases up to 0.3564, one eigenvalue becomes positive and the homogeneous regime loses its stability via a supercritical pitchfork bifurcation at $BP1$ dictating a Turing instability which gives rises to two branches of inhomogeneous stable asymmetric (conjugate) solutions. A representative profile of these solutions is shown in Fig. 8b. On each one of these branches, a stable periodic regime appears through a supercritical Andronov–Hopf bifurcation at $L = 0.385$ ($H1$) which ends at a Andronov–Hopf bifurcation at $L = 0.886$ ($H2$). Representative oscillating profiles for $L = 0.65$ are reported in Fig. 8c at different time instances within one period.

After the Andronov–Hopf bifurcation ($H2$) the inhomogeneous time invariant solutions gain stability until $L = 2.903$ ($LP1$) where both asymmetric branches lose their stability via a saddle–node bifurcation. Past the turning point, one of the branches bifurcates through a transcritical bifurcation ($BP7$) at $L = 2.108$ from the upper branch of the far-from-equilibrium (inhomogeneous) solutions (see Fig. 6).

The second pair of branches of unstable inhomogeneous solutions arise through a pitchfork bifurcation at $L = 0.712$ ($BP2$) where a

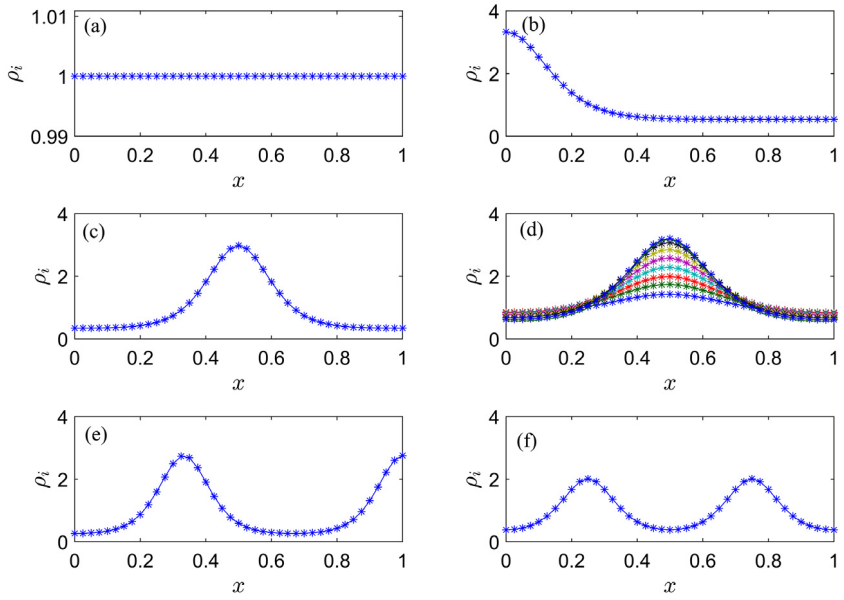

Fig. 5. Characteristic profiles of solutions of the bifurcation diagram shown in Fig. 4. (a) A stable homogeneous solution. (b) A stable inhomogeneous solution (first bifurcating branch). (c) Unstable inhomogeneous solution (second bifurcating branch). (d) A time periodic solution (second bifurcating branch). (e), (f) Unstable inhomogeneous solutions corresponding to third and fourth bifurcating branches.

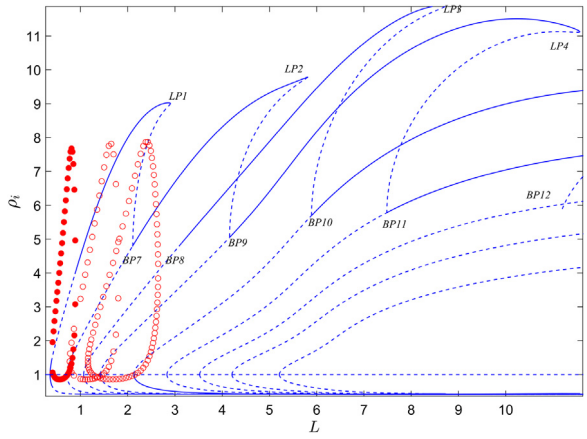

Fig. 6. Bifurcation diagram with respect the size of the domain L. For higher values of L, the system displays several branches of solutions. As the value of L decreases branches of limit cycles arise. For values less than the critical value $L = 0.3564$, only homogeneous solutions exist.

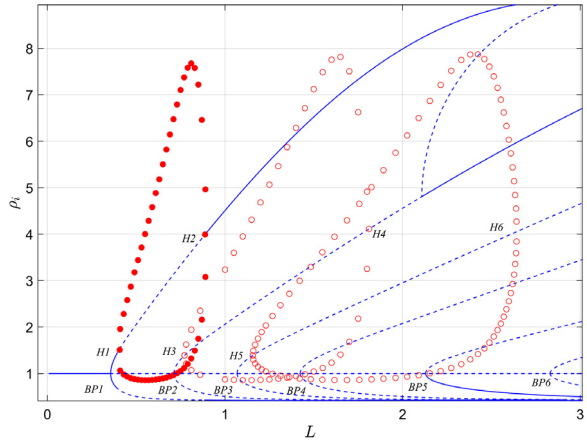

Fig. 7. Bifurcation diagram with respect the size for $0 < L \leq 3$.

second symmetry-breaking (with respect to the homogeneous solution) bifurcation occurs (a second eigenvalue passes through zero). One of the two representative symmetric profiles for $L = 1.211$ is shown in Fig. 8d. On this branch of inhomogeneous solutions, a further increase of the bifurcation parameter L leads to an Andronov–Hopf bifurcation at $L = 0.772$ marked as ($H3$) in Fig. 7, which gives rise to stable (on one branch) and unstable (on the other branch) limit cycles. These time-periodic solutions disappear at $L = 1.785$ via a second Andronov–Hopf bifurcation marked as ($H4$) in Fig. 7. Characteristic time-oscillating profiles in periodic regimes arising from the first Andronov–Hopf bifurcation ($H3$) are depicted in Fig. 8e (as snapshots within the period). After the second Andronov–Hopf bifurcation ($H4$), the branch of time-invariant inhomogeneous solutions remains unstable and gains stability at the bifurcation $BP7$. This solution remains stable until $L = 5.808$ where loses stability via a saddle–node bifurcation (marked as ($LP2$) in Fig. 6). The bifurcating branch from the $LP2$ turning point meets a transcritical bifurcation ($BP9$) at $L = 4.155$.

Between the $H3$ and $H4$ Andronov–Hopf bifurcations, a symmetry breaking occurs at the homogeneous branch. Specifically, on the homogeneous branch, a new leading eigenvalue becomes positive at $L = 1.1301$ and a pitchfork bifurcation ($BP3$) occurs. At this point, two new unstable branches of inhomogeneous regimes arise. Representative profiles for $L = 1.538$ are shown in Fig. 8f. Then, a similar picture comes forward: as L increases, unstable periodic solutions (for both branches) are born and die through two Andronov–Hopf bifurcations ($H5$) and ($H6$), respectively.

The upper part of the third in the series bifurcating branch gains stability at $L = 3.143$ ($BP8$) which holds on until a saddle–node bifurcation ($LP3$) at$L = 8.718$ where the branch bifurcates to saddles. This branch meets another transcritical bifurcation at $L = 5.8907$ (marked as ($BP10$) in Fig. 6).

The succeeding 4th, 5th, 6th bifurcating branches reveal similar dynamics: successive symmetry-breaking from the homogeneous solution, leading to unstable solutions. These branches gain stability through transcritical bifurcations which connect previous unstable branches: branch 2 meets branch 4, branch 3 meets branch 5, branch 4 meets branch (6) at the critical points $BP9, BP10, BP11$ (corresponding to $L = 4.155, L = 5.8907, L = 7.484$), respectively.

It should be observed that multiplicity of stable solutions exists for a wide range of the bifurcation parameter L. For example, co-existence

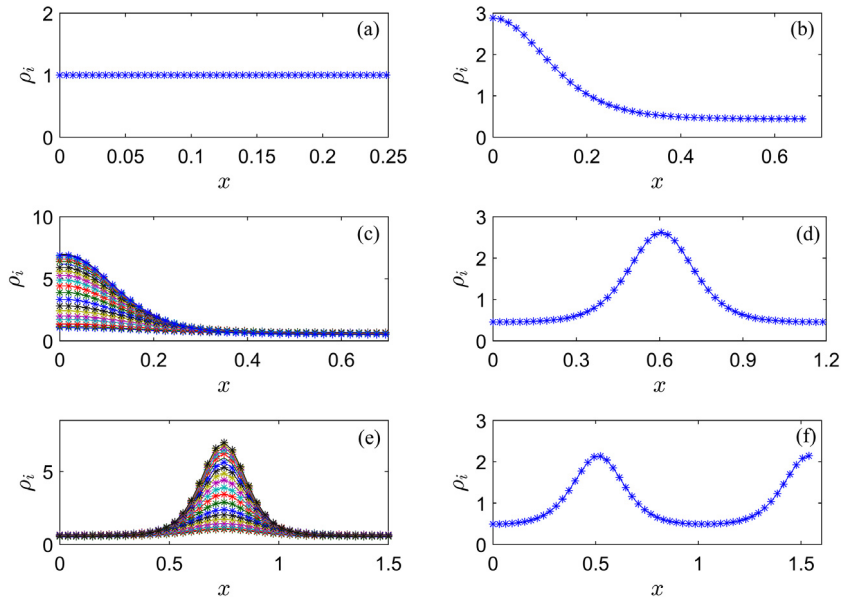

Fig. 8. Characteristic profiles of solutions from the bifurcation diagram shown in Fig. 7. (a) A Homogeneous solution. (b) A stable inhomogeneous solution (first bifurcating branch). (c) A stable time periodic inhomogeneous solution (first bifurcating branch). (d) An unstable inhomogeneous solution (second bifurcating branch). (e) A stable time periodic inhomogeneous solution (second bifurcating branch). (f) An unstable inhomogeneous solution corresponding (third bifurcating branch).

of an inhomogeneous steady state and a limit cycle is observed between the $LP1$ point and $H4$ bifurcation, whereas beyond the critical value of the $H4$ point there is a co-existence of two inhomogeneous regimes (shown in Fig. 8b and d, respectively).

We highlight the complexity of the dynamic behavior as L increases. For example, between $BP11$ and $LP3$ there are eight (four plus four due to symmetry) stable inhomogeneous solutions which coexist with six (three plus three due to symmetry) unstable inhomogeneous solutions.

Fig. 9 shows the two stable (conjugate) solutions for the second, fourth, fifth and sixth branches.

As shown in Section 5, the first bifurcation from the homogeneous solution (i.e. at the critical point $BP1$) can be found by solving Eqs. (17)–(18). For $\beta = 1.8$, Eqs. (17)–(18) give:

$$a + \frac{a\gamma\rho_{0i}^2 L^2}{D_m\pi^2} + D_i\left(\frac{\pi}{L}\right)^2 + \frac{D_i}{D_m}\gamma\rho_{0i}^2 = \beta \Leftrightarrow \frac{L^2}{\pi^2} + 0.01\left(\frac{\pi}{L}\right)^2 - 1.79 = 0$$
$$\Rightarrow L = 0.3564$$

which is in excellent agreement with the numerical results. Linear stability theory, predicts that as L decreases, the critical value for the first Turing instability increases, while, the critical value of the first Andronov–Hopf bifurcation $\beta_H^C = \gamma\rho_{0i}^2 + a$ is independent from the size L. If we start with β such that, $\beta_T^C(L) < \beta_H^C < \beta$ then as $\beta_T^C(L)$ increases, at some critical value this implies $\beta_H^C < \beta = \beta_T^C(L)$. For lower values of L, the sufficient conditions for the time periodic homogeneous solutions is satisfied. Fig. 10a shows the temporal evolution of the homogeneous periodic profile for $L = 0.1$ and $\beta = 4$ while Fig. 10b depicts the evolution of the time periodic inhomogeneous solution for $L = 1.6$ and $\beta = 1.8$.

8. Symmetry properties of the dislocations patterns

It is well known that in far-from-equilibrium states, self-organized phenomena are often coupled with symmetry-breaking phenomena. In this section, we discuss the problem of symmetry within the framework of reaction–diffusion models arising from the modeling of dislocations patterning phenomena, which are themselves examples of mechanisms for generating asymmetric structures.

The interest in symmetry-breaking arises primarily from the fact that the emergence of order is often accompanied by the appearance of spatially asymmetric patterns. Such symmetry-breaking phenomena are therefore of special interest in modeling the behavior of complex phenomena in material science where both order and asymmetry are ubiquitous.

Let us consider Eq. (1) in more abstract form as follows:

$$\begin{cases} \dfrac{\partial\boldsymbol{\rho}}{\partial t} = \mathbf{D}\dfrac{\partial^2\boldsymbol{\rho}}{\partial x^2} + \mathbf{R}(\boldsymbol{\rho}) \\ \dfrac{\partial\boldsymbol{\rho}}{\partial x}(0,t) = \dfrac{\partial\boldsymbol{\rho}}{\partial x}(L,t) = 0 \end{cases} \tag{27}$$

where $\boldsymbol{\rho}$ is the vector of the dislocations densities, $\mathbf{D}$ the diffusion matrix, and $\mathbf{R}$ a vectorial nonlinear function. As we pointed out already, such a system admits at least one uniform steady-state solution, which is usually regarded as a "reference" state describing the total absence of self-organization. In addition to this solution, one may have bifurcations of space-dependent solutions. However, for every non-uniform solution $\boldsymbol{\rho}(x,t)$, in which x is the space coordinate, there exists a solution $\boldsymbol{\rho}(x',t)$, in which x' is obtained from x by the action of a symmetry group G:

$$x' = \gamma x \ \forall\gamma \in G. \tag{28}$$

This solution has stability properties identical to those of $\boldsymbol{\rho}(x,t)$.

The group G is compatible with the geometry and the boundary conditions and commutes with the Laplace operator. In our case, it is well known that Neumann boundary conditions (NBC) generate symmetries in reaction–diffusion equations. Moreover, if the problem is extended in the domain $[-L\ L]$ with periodic boundary conditions, the symmetries are the ones of the circle, that is O(2) symmetries, and it can be demonstrated that the solutions are in one to one correspondence with the NBC problem over the domain $[0\ L]$.

Here, we only analyze the reflection symmetry Z_2 of the reaction–diffusion problem with the Neumann boundary conditions on the domain $[0\ L]$. Indeed, it is easy to show that Eq. (27) with the boundary conditions are invariant under the transformation:

$$x \to L - x. \tag{29}$$

Thus, steady state profiles may be invariant or not with respect to this transformation. Examples of symmetric profiles are reported in Fig. 9a, b, d respectively, whereas examples of asymmetric profiles are reported in Fig. 11a, b. With respect to symmetry, all the solutions transformed

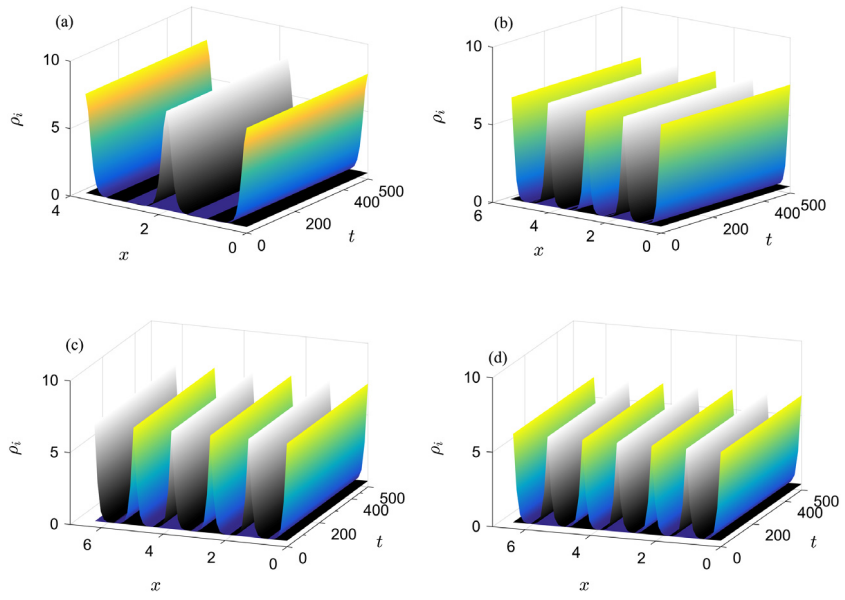

Fig. 9. Profiles of the stable solutions of the bifurcation diagrams shown in Figs. 6, 7 for the bifurcating branches 2, 4, 5 and 6 respectively. Each plot contains two conjugate solutions (color versus gray scale). As the value L increases we observe a nucleation of spikes for the density of immobile dislocations ρ_i. (For interpretation of the references to color in this figure legend, the reader is referred to the web version of this article.)

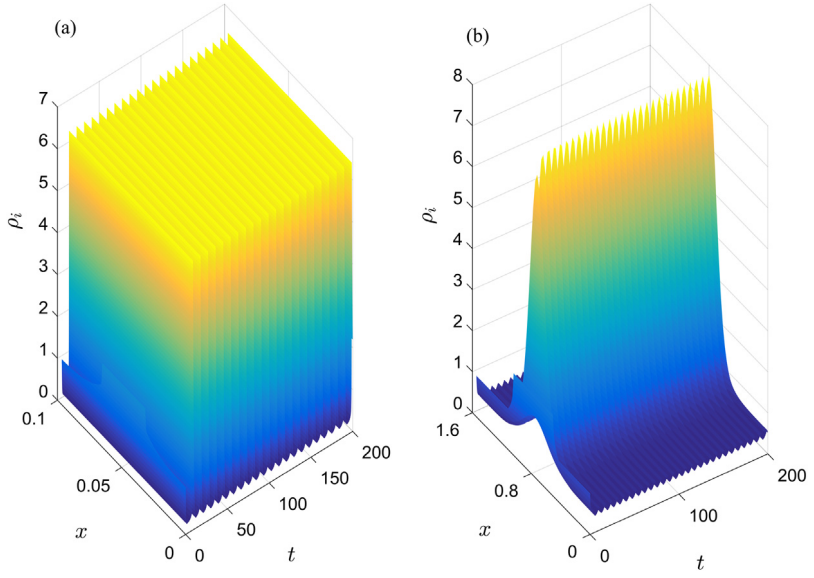

Fig. 10. Stable homogeneous versus inhomogeneous time periodic solutions. (a) For $L = 0.1$ and $\beta = 4$. (b) A time periodic inhomogeneous profile for $L = 1.6$ and $\beta = 1.8$.

by Eq. (29) must be also solutions of the equations. Thus, in the presence of asymmetric solutions, multiplicity is forced by the symmetry action. An illustration of the multiplicity due to the invariance properties of Eq. (27) under reflection with respect to an axis passing through the center of symmetry of the system is indeed shown in Fig. 11. Both $\rho(x)$ and its mirror image $\gamma\rho(x)$ (also called γ-*conjugate* steady states) exist and have identical stability properties.

Thus, in the case of reflection symmetry, asymmetric solutions come in pairs as it is shown in Figs. 9 and 11. As a consequence of the system symmetry, in reaction–diffusion equations with NBC on [0 L], like Eq. (27), the generic steady-state bifurcation from the trivial solution is always a pitchfork (corollary 7.3 page. 206 in [71]).

The system's symmetry also affects the periodic regimes which may be invariant or not with respect to the reflection transformation. Suppose that $x(t)$ is a T-periodic solution of Eq. (27) and let us call $\gamma \epsilon Z_2$ the reflection transformation Eq. (28). Then for the equation symmetry, $\gamma x(t)$ is another T-periodic solution of Eq. (27). For the uniqueness of the solutions, either the two trajectories $\gamma x(t)$ and $x(t)$ are identical or they do not intersect. In the case where $\gamma x(t)$ and $x(t)$ are two different trajectories, then $x(t)$ is asymmetric and $\gamma x(t)$ is the γ-conjugate solution which is obtained by its reflection. This is the case reported in Fig. 12a where two limit cycles are born from asymmetric γ-conjugate steady state solutions coming in pair. Thus, a multiplicity of asymmetric γ-conjugate limit cycles is observed.

In the case where the two trajectories coincide, then there is a unique symmetric limit cycle. In particular, symmetric limit cycles may be of two kinds: point-wise invariant or set-wise invariant. In the first case, each point of the limit cycle is invariant under the action of Eq. (28). That is: $\gamma x(t) = x(t)\ \forall t$. An example of this property is the periodic solution reported in Fig. 12b. In this case, the spatial profile is at each

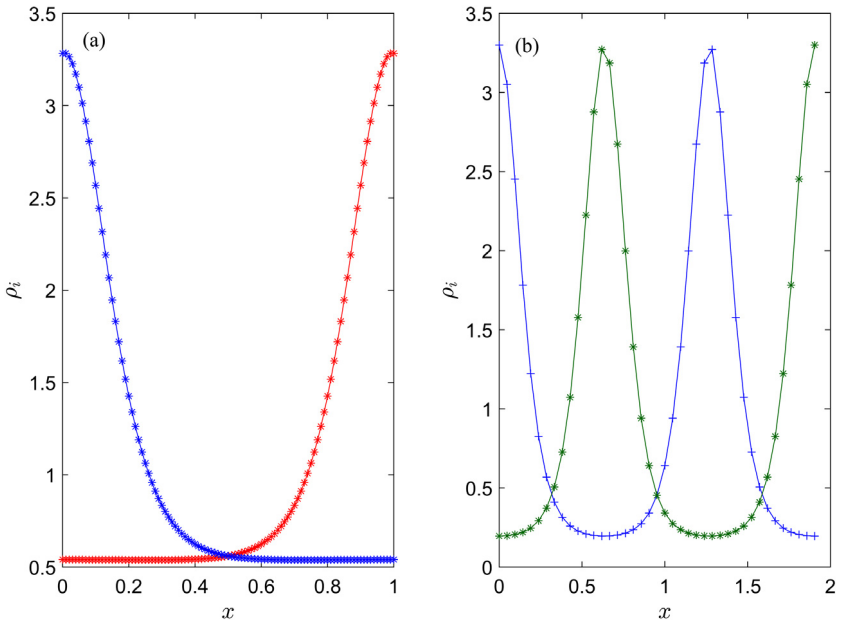

Fig. 11. Two examples of multiplicity due to system symmetry. (a) Asymmetric regimes arising from the BP1 in Fig. 4. (b) Asymmetric regimes arising from the *BP*4 in Fig. 4. Both $\rho(x)$ and its mirror image $\gamma\rho(x)$ exist and have identical stability properties. Similar symmetry breaking phenomena are observed in correspondence of *BP*1 and *BP*3 in Fig. 7.

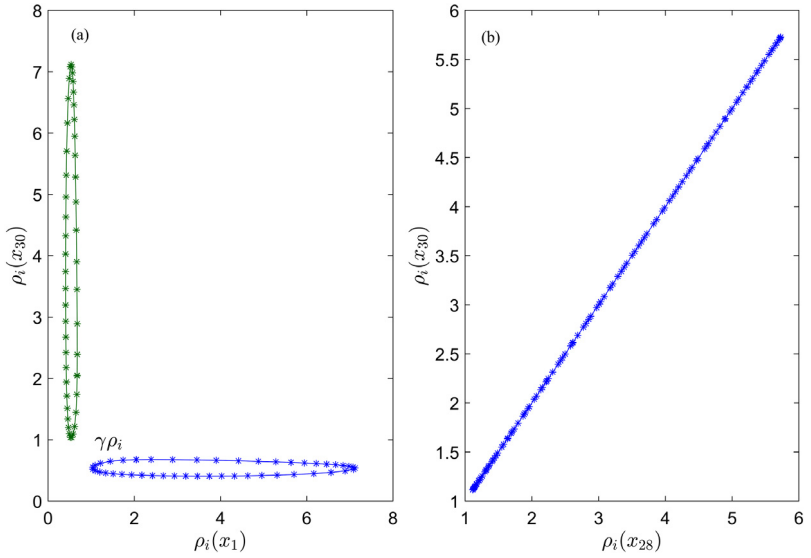

Fig. 12. Symmetry property of the periodic regimes. (a) A couple of γ-conjugate asymmetric periodic regimes arising from the H1 point in Fig. 7. (b) A spatial symmetric periodic regime arising from the H3 point in Fig. 7.

time t invariant with respect to the action of Eq. (28). This symmetry is also called spatial symmetry. In the second case, there exists a time translation θ such that $\gamma x(t) = x(t-\theta)$. In general, for reflection symmetry it holds that $\theta = \frac{1}{2}T$ where T is the orbit period. This symmetry is also called spatio-temporal symmetry. At the current work, we did not observe these kinds of periodic regimes in our numerical analysis.

9. Conclusions

We analyzed the dynamics of pattern formation of the initial WA model for dislocation patterning under cyclic loading. The rich nonlinear dynamics of the model is related to the plastic deformation of material being a high nonlinear far-from- equilibrium dissipative process. We found several criticalities, for both the shear stress dependent β and the size of the domain L, which mark the onset of (micro material) instabilities and phase transitions. The localization of the density of dislocations as follows from analysis with respect to the β parameter and the size of the domain L is related with the PSB formation.

The size effect reflects the competition between finite geometry i.e. the external length and the intrinsic (internal) length [60,72]. It is worth noting the phenomenological similarity between experimental results (both for monotonic and cyclic) deformations and our theoretical and numerical findings with respect to the size effect. In particular, studies have revealed that the yield stress (in the stress strain curve) increases dramatically as the diameter of the domain decreases, so that PSBs are difficult to be observed for small domain sizes and fewer slip bands form [64–68]. For example, it has been shown that the critical grain size for the appearance of stable PSB patterns formation is ~25 μm for CG-Cu. A similar size effect was reported in [68] during the cycle deformation of polycrystalline thin film. It was found that thinner

films are more resistant to fatigue, while the critical value of yield stress increases as the diameter of the specimen decreases. In an analogy to the above findings, our analysis suggests that the critical value of the shear stress (β_T^C) where the first plastic (Turing) instability occurs, also increases abruptly as the size of the domain L decreases (namely inversely with the L^2). Furthermore, as our linear and numerical bifurcation analysis (Figs. 6–7) suggests, as the size L decreases there are fewer branches of inhomogeneous solutions. Finally, we showed that as the size of the domain decreases below a critical value, the system is trapped in the homogeneous branch of solutions (we can say that the geometry wins). On the contrary, as the size increases several criticalities drive the system to complex dynamics and far-from-equilibrium pattern formation.

Numerical bifurcation analysis allowed us to detect several branches of far-from-equilibrium solutions as they result from symmetry-breaking bifurcations of Turing instabilities leading to different pattern formations. Furthermore, we detected Andronov–Hopf bifurcations on far-from-equilibrium branches of solutions giving rise to periodically oscillating patterns. The time oscillatory behavior of mobile dislocations has been observed in pinned oscillations [73] and in other processes such us irradiation [74] and melting–solidification [75]. The Andronov–Hopf bifurcations that give birth to far-from-equilibrium nonlinear oscillations are one of the essential criticalities that are connected with phenomena such as bursting that have been observed in experiments during cyclic deformation [76]. Here, we should note that nonlinear oscillations for the WA model have been also reported for example in [60,70]. However these correspond to nonlinear oscillations of the homogeneous solutions and not of far-from-equilibrium patterns which are reported here for the first time.

It should be emphasized that the oscillating solutions appearing in our model may be the result of the interaction between the Turing and Andronov–Hopf instabilities of the homogeneous state. Many studies have been focused on the dynamics resulting from the coupling between these two different instabilities including experimental and theoretical results in different fields [77]. Indeed, Turing bifurcation breaks just the spatial symmetry of the homogeneous state, whereas the Andronov–Hopf bifurcation breaks just the temporal one leading the solution to a homogeneous but periodic state. Moreover, while the condition for Turing instabilities is the result of the interplay of the different diffusivities of the activator/inhibitor and the nonlinearities, the Andronov–Hopf instabilities are connected just to the nonlinearities of the system. Nevertheless, for some parameter values both the conditions may be satisfied leading to a codimension two Turing–Andronov–Hopf point (CTHP) [78,79]. Close to this CTHP point, the competition between the spatial and the temporal modes may give rise to a variety of complex spatiotemporal behavior which includes bistability between pure Turing and pure homogeneous periodic states, localized structures where both behaviors are possible along the domain, subharmonic Turing patterns or oscillating Turing patterns. From the linear stability analysis at the CTHP, two conditions are met: a real root vanishing for a wave number kc and a pair of complex conjugate roots with zero real part and frequency ωc. These two conditions lead or to the spatial Turing mode characterized by the wavenumber frequency couple (k_c, 0) or the temporal Andronov–Hopf mode (0, ω_c). From the amplitude equations analysis [80], three different solutions are possible: the pure Turing modes, the pure Andronov–Hopf modes or the mixed modes (k_c, ω_c) consisting of Turing patterns oscillating globally in time [81]. However, the stability of these states is different in the parameter range. Two are the possibilities: or both Turing and Andronov–Hopf modes are stable and the mixed modes are unstable or the mixed modes are stable when both the Turing and Andronov–Hopf are unstable. Thus, in the vicinity of the CTHP point the system may exhibit either bistability between steady Turing patterns and temporal periodic regimes or a variety of mixed mode states ranging from the simple Turing oscillating patterns to different patterns characterized by alternated subharmonic Turing modes and oscillating structures. In our case, the oscillating patterns arise from Andronov–Hopf bifurcations on Turing branches thus resembling the same average spatial structure of the Turing pattern but oscillating in time. We also note that the Andronov–Hopf bifurcations are always very close to the Turing bifurcation points which indicate that we are very close to a CTHP point. However, a systematic analysis of the interaction between the Turing and Andronov–Hopf modes is behind the scope of the paper and it will be the object of a future work.

Further research could proceed along several directions including the analysis of dynamics with respect the other parameters of the model (for example, the influence of diffusion parameters as a function of stress), and the 2D bifurcation analysis of the dimensionless model. Another direction in the dislocation patterning could be the use of different types of (non singular) solutions for the displacement field in the DDD models resulting from Gradient Elasticity theory [1]. Then a different statistical analysis for the dislocations densities could be attempted. Finally, the effort to bridge mesoscopic modeling and description (i.e. DDD models) with the continuum description of WA model with the use of new computational methodologies (such us Equation Free Methodology [58,59]). One of the most critical issues is related to the bridging of the different spatial and temporal scales: the nano/micro-scale, and that of the meso and macroscopic scale where the dynamic behavior of the material emerges. Traditionally, the gap between the microscopic and macroscopic level is bridged through closures, relating higher-order moments of the underlying distributions to a few, lower-order moments. However, such closures are often based on various assumptions that may impose biases for the analysis at the macroscopic level. Thus, heterogeneities, nonlinearities and stochastic interactions put limitations when trying to systematically bridge the different time and spatial scales. The Equation-free methodology is a mathematical/numerical assisted multiscale framework that provides an alternative way to bridge the interaction of "microscopic agents"—such as dislocations, in order to analyze the macroscopic dynamics bypassing the need to extract analytical closures. Thus using the microscopic simulator as a black-box numerical experiment one can perform various system-level tasks such as numerical bifurcation analysis as well rare-event analysis.

Acknowledgments

Financial support has been provided by EΣΠA and ERC-13 project (IL-GradMech-ASM, 88257). At latest stages this work was partly supported by a Mega Grant (No. 14.Z50.31.0039) of the Russian Ministry of Education to Togliatti State University and a grant from the Greek Secretariat of Research and Technology.

References

[1] E.C. Aifantis, Gradient deformation models at nano micro and macro scales, J. Eng. Mater. Technol. 121 (1999) 189–202.
[2] G. Ananthakrishna, Current theoretical approaches to collective behavior of Dislocations, Phys. Rep. 440 (2007) 113–259.
[3] D. Walgraef, E.C. Aifantis, Plastic instabilities, dislocation patterns and nonequilibrium phenomena, Res. Mech. 23 (1988) 161–195.
[4] D. Walgraef, E.C. Aifantis, Dislocation patterning in fatigued metals as a result of dynamical instabilities, J. Appl. Phys. 58 (1985) 688–691.
[5] M. Zaiser, E.C. Aifantis, Avalanches and slip patterning in plastic deformation, J. Mech. Behav. Mater. 14 (2003) 255–270.
[6] E.C. Aifantis, Non-linearity, periodicity and patterning in plasticity and fracture, Internat. J. Non-Linear Mech 31 (1996) 797–809.
[7] K. Yagasaki, Bifurcations and chaos in vibrating microcantilevers of tapping mode atomic force microscopy, Internat. J. Non-Linear Mech 42 (2007) 658–672.
[8] G. Ananthakrishna, Dislocation dynamics and chaos, Solid State Phenom. 23–24 (1992) 417–427.
[9] F. Csikor, C. Motz, D. Weygand, M. Zaiser, S. Zapperi, Dislocation avalanches, strain bursts, and the problem of plastic forming at the micrometer scale, Science 307 (2007) 251–254.
[10] T. Tabata, H. Fujita, M.A. Hiraoka, K. Onishi, Dislocation behaviour and the formation of persistent slip bands in fatigued copper single crystals observed by high-voltage electron microscopy, Phil. Mag. A 43 (1983) 841–857.
[11] J.P. Perdew, A. Zunger, Self-interaction correction to density-functional approximations for many-electron system, Phys. Rev. B 23 (1981) 5048.

[12] P. Hohenberg, W. Kohn, Inhomogeneous electron gas, Phys. Rev. 136 (1964) B864–871.
[13] S. Frederiksen, K. Jacobsen, Density functional theory studies of screw dislocation core structures in bcc metals, Phil. Mag. 83 (2003) 365–375.
[14] J. Chang, W. Cai, V. Bulatov, Molecular dynamics simulations of motion of edge and screw dislocations in a metal, Comput. Mater. Sci. 23 (2002) 111–115.
[15] K. Lin, D. Chrzan, Kinetic Monte Carlo simulation of dislocation dynamics, Phys. Rev. B 60 (1999) 3799–3805.
[16] J. Lepinoux, L. Kubin, The dynamic organization of dislocation structures: a simulation, Scr. Metall. 21 (1987) 833–838.
[17] A. Gulluoglu, D. Srolovitz, R. LeSar, P.S. Lomdahl, Dislocation distributions in two dimensions, Scr. Metall. 23 (1989) 1347–1352.
[18] E. Giessen, A. Needleman, Discrete dislocation plasticity: A simple planar model, Mater. Sci. Eng. 3 (1995) 689–735.
[19] E. Giessen, A. Needleman, Micromechanics simulations of fracture, Annu. Rev. Mater. Res. 32 (2002) 141–162.
[20] M. Rhee, H. Zbib, J. Hirth, H. Huang, T.D. Rubia, Models for long-/short-range interactions and cross slip in 3D dislocation simulation of BCC single crystals, Modelling Simul. Mater. Sci. Eng. 6 (1998) 467–492.
[21] V. Gregor, J. Kratochvil, Self-organization approach to cyclic microplasticity: A model of a persistent slip band, Int. J. Plast. 14 (1998) 159–172.
[22] I. Groma, Link between the microscopic and mesoscopic length-scale description of the collective behavior of dislocations, Phys. Rev. B 56 (1997) 5807–5813.
[23] I. Groma, B. Bakó, Dislocation patterning: From micro–to mesoscale description, Phys. Rev. Lett. 84 (2000) 1487.
[24] M. Zaiser, M. Miguel, I. Groma, Statistical dynamics of dislocation systems: The influence of dislocation–dislocation correlations, Phys. Rev. B 64 (2001) 1–9.
[25] I. Groma, M. Zaiser, P.D. Ispanovity, Dislocation patterning in a two-dimensional continuum theory of dislocations, Phys. Rev. Lett. B 93 (2016) 214110.
[26] A. Azab, Statistical mechanics of dislocation systems, Scr. Mater. 54 (5) (2006) 723–727.
[27] T. Hochrainer, M. Zaiser, P. Gumbsch, A three-dimensional continuum theory of dislocation systems: Kinematics and mean field formulation, Phil. Mag. 87 (2007) 1261–1282.
[28] S. Sandfeld, M. Zaiser, Pattern formation in a minimal model of continuum dislocation plasticity, Modelling Simul. Mater. Sci. Eng. 23 (2015) 065005.
[29] S. Xia, A. Azab, Computational modelling of mesoscale dislocation patterning and plastic deformation of single crystals, Modelling Simul. Mater. Sci. Eng. 23 (2015) 055009.
[30] N. Grilli, K.G.F. Janssens, J. Nellessen, S. Sandlobes, D. Raabe, Multiple slip dislocation patterning in a dislocation-based crystal plasticity finite element method, Int. J. Plast. 100 (2018) 104–121.
[31] D. Walgraef, E.C. Aifantis, On certain problems of deformation-induced material instabilities, Internat. J. Engrg. Sci. 59 (2012) 140–155.
[32] D. Walgraef, E.C. Aifantis, On the formation and stability of dislocation patterns -I, Internat. J. Engrg. Sci. 23 (1985) 1351–1358.
[33] N. Ghoniem, E. Busso, N. Kioussis, H. Huang, Multiscale modelling of nanomechanics and micromechanics: an overview, Phil. Mag. 83 (2003) 3475–3528.
[34] A. Ord, B. Hobbs, Fracture pattern formation in frictional, cohesive, granular material, Phil. Trans. R. Soc. A 368 (2010) 95–118.
[35] J. Xu, G. Zhang, Effects of grain size and initial immobile dislocation density on fatigue behavior of polycrystalline metals, Mater. Sci. Eng. A 590 (2014) 194–198.
[36] G. Nicolis, I. Prigogine, Self-Organization in Nonequilibrium Systems: From Dissipative Structures to Order Through Fluctuations, Wiley, 1977.
[37] G. Nicolis, P. Gaspard, Bifurcations, chaos and self-organization in reaction–diffusion systems, in: D. Roose, B. de Dier, A. Spence (Eds.), Continuation and Bifurcations: Numerical Techniques and Applications, Kluwer Academic Publishers, Dordrecht, 1990, pp. 43–70.
[38] A.M. Turing, The chemical basis of morphogenesis, Phil. Trans. R. Soc. B 237 (1952) 37–72.
[39] L. Yang, M. Dolnik, A.M. Zhabotinsky, I.R. Epstein, Spatial resonances and superposition patterns in a reaction-diffusion model with interacting turing modes, Phys. Rev. Lett. 88 (2002) 208303.
[40] L. Yang, I.R. Epstein, Oscillatory turing patterns in reaction-diffusion systems with two coupled layers, Phys. Rev. Lett. 90 (2003) 178303.
[41] V.K. Vanag, I.R. Epstein, Out-of-phase oscillatory Turing patterns in a bistable reaction–diffusion system, Phys. Rev. E 71 (2005) 066212.
[42] Y. Kuramoto, Chemical Oscillations, Waves and Turbulence, Springer, 1984.
[43] L.F. Olsen, H. Degn, Chaos in biology systems, Q. Rev. Biophys. 18 (1985) 165–225.
[44] J.D. Murray, Mathematical Biology, Springer, 2002.
[45] A. Winfree, Varieties of spiral wave behavior: an experimentalist's approach to the theory of excitable media, Chaos 1 (3) (1991) 303–334.
[46] I. Lengyel, I. Epstein, Systematic design of chemical oscillations—a chemical approach to designing Turing patterns in reaction–diffusion systems, Proc. Natl. Acad. Sci. USA 89 (9) (1992) 3977–3979.
[47] M. Cross, P. Hohenberg, Pattern formation outside equilibrium, Rev. Modern Phys. (65) (1993) 851–1112.
[48] P. Maini, K. Painter, H. Chau, Spatial pattern formation in chemical and biological systems, J. Chem. Soc. Faraday Trans. 93 (20) (1997) 3601–3610.
[49] R.K. Upadhyay, P. Roy, J. Datta, Complex dynamics of ecological systems under nonlinear harvesting: Hopf bifurcation and Turing instability, Nonlinear Dynam. 79 (2015) 2251–2270.
[50] F. Rao, Spatiotemporal complexity of a three-species ratio-dependent food chain model, Nonlinear Dynam. 76 (3) (2014) 1661–1676.
[51] T. Zhang, Y. Xing, H. Zang, M. Han, Spatio-temporal dynamics of a reaction–diffusion system for a predator–prey model with hyperbolic mortality, Nonlinear Dynam. 77 (2014) 1–13.
[52] J.L. Aragon, R.A. Barrio, T.E. Woolley, R.E. Baker, P.K. Maini, Nonlinear effects on Turing patterns: Time oscillations and chaos, Phys. Rev. E 86 (2012) 026201.
[53] M.L. Kavousanakis, L. Russo, C.I. Siettos, A.G. Boudouvis, G.C. Georgiou, A timestepper approach for the systematic bifurcation and stability analysis of polymer extrusion dynamics, J. Non-Newton. Fluid Mech. 151 (2008) 59–68.
[54] H.B. Keller, Numerical solution of bifurcation and non-linear eigenvalue problems, in: P.H. Rabinowitz (Ed.), Applications of Bifurcation Theory, Academic Press, New York, 1977, pp. 359–384.
[55] Y. Kuznetsov, Elements of Applied Bifurcation Theory, Springer, 2004.
[56] A. Dhooge, W. Govaerts, Y.A. Kuznetsof, MatCont: A Matlab package for numerical bifurcation analysis of ODEs, ACM Trans. Math. Softw. 29 (2013) 141–164 (2003).
[57] R. Seydel, Practical Bifurcation and Stability Analysis, Springer, 2010.
[58] I.G. Kevrekidis, C.W. Gear, J.M. Hyman, P.G. Kevrekidis, O. Runborg, C. Theodoropoulos, Equation-free, coarse-grained multiscale computation: Enabling mocroscopic simulators to perform system-level analysis, Commun. Math. Sci. 1 (4) (2003) 715–762.
[59] C.I. Siettos, M. Graham, I.G. Kevrekidis, Coarse Brownian dynamics for nematic liquid crystals: Bifurcation, projective integration, and control via stochastic simulation, J. Chem. Phys. 118 (2003) 10149–10156.
[60] M. Glazov, L.M. Llanes, C. Laird, Self-organized dislocation structures (SODS) in fatigued metals, Phys. Status Solidi A 149 (1995) 297–321.
[61] D. Walgraef, E.C. Aifantis, On dislocation patterning: Revisiting the W-A model part I: The role of gradient terms in dislocation dynamics, J. Mech. Behav. Mater. 19 (1) (2009) 49–66.
[62] O.B. Pedersen, A.T. Winter, Cyclic hardening and slip localization in single slip oriented copper crystals, Phys. Status Solidi (A) 149 (1995) 281–296.
[63] H. Huang, N. Ghoniem, T.D. de la Rubia, M. Ree, H.M. Zbib, J.P. Hirth, Stability of dislocation short-range reactions in bcc crystals, J. Eng. Mater. Technol. 121 (1999) 143–150.
[64] H. Kawazoe, M. Yoshida, Z.S. Basinski, M. Niewczas, Dislocation microstructures in fine-grained Cu polycrystals fatigued at low amplitude, Scr. Mater. 42 (1999) 639–644.
[65] Q.S. Pan, L. Lu, Strain-controlled cyclic stability and properties of Cu with highly oriented nanoscale twins, Acta Mater. 81 (2014) 248–257.
[66] M.D. Uchic, D.M. Dimiduk, J.N. Florando, W.D. Nix, Sample dimensions influence strength and crystal plasticity, Science 305 (2004) 986–989.
[67] Y. Wang, J. Li, A.V. Hamza, T.W. Barbee, Ductile crystalline-amorphous nanolaminates, Proc. Natl. Acad. Sci. USA 104 (2007) 11155–11160.
[68] R. Schwaigery, G. Dehm, O. Kraft, Cyclic deformation of polycrystalline Cu films, Phyl. Mag. 83 (6) (2003) 693–710.
[69] R. Peng, M. Wang, Pattern formation in the Brusselator system, J. Math. Anal. Appl. 309 (2005) 151–166.
[70] C. Schiller, D. Walgraef, Numerical simulation of persistent slip band formation, Acta Metall. 36 (3) (1988) 563–574.
[71] M. Golubitsky, I. Stewart, The Symmetry Perspective from Equilibrium to Chaos in Phase Space and Physical Space, Vol. 200, Springer, 2002.
[72] X. Zhang, K. Aifantis, Interpreting the internal length scale in strain gradient plasticity, Rev. Adv. Mater. Sci. 41 (2015) 72–83.
[73] M. Bhattacharya, A. Dutta, P. Mukherjee, N. Gayathri, P. Bara, Inertial oscillations of a pinned dislocation, Phys. Rev. B 82 (2010) 184113.
[74] S. Murphy, Spatial instability in dislocation structure under irradiation, Europhys. Lett. 3 (1987) 1267–1272.
[75] O. Barabash, S. Babu, J.M. Vitek, S. David, G.E. Ice, R.I. Barabash, Unusual dislocation density oscillations after local melting and solidification of Ni-based superalloys, TMS Lett. (2005).
[76] P. Neumann, Coarse slip model of fatigue, Acta Metall. (17) (1969) 1219–1225.
[77] M.C. Cross, P.C. Hohenberg, Pattern formation outside of equilibrium, Rev. Modern Phys. 65 (1993) 851–1112.
[78] A. De Wit, D. Lima, G. Dewel, P. Borckmans, Spatiotemporal dynamics near a codimension-two point, Phys. Rev. E 54 (1996) 261–271.
[79] M. Meixner, A. De Wit, S. Bose, E. Scholl, Generic spatiotemporal dynamics near codimension-two Turing–Hopf bifurcations, Phys. Rev. E 55 (1997) 6690–6697.
[80] J. Guckenheimer, P. Holmes, Nonlinear Oscillations, Dynamical Systems, and Bifurcations of Vector Fields, Springer-Verlag, 1983.
[81] A. De Wit, G. Dewel, P. Borckmans, Chaotic Turing–Hopf mixed mode, Phys. Rev. E 48 (1993) 4191–4195.